Deep learning versus the human visual system for detecting motion blur in radiography

Rie Tanaka[a,*] **Shiho Nozaki**[b] **Futa Goshima**[b] **and Junji Shiraishi**[c]
[a]Kanazawa University, College of Medical, Pharmaceutical and Health Sciences, Kanazawa, Japan
[b]Kanazawa University, Graduate School of Health Sciences, Kanazawa, Japan
[c]Kumamoto University, Faculty of Life Sciences, Kanazawa, Japan

Abstract

Purpose: The necessity of image retakes is initially determined on a preview monitor equipped with an operating system; therefore, some image blurring is only noticed later, on a high-resolution monitor. The purpose of this study is to investigate blur detection performance on radiographs via a deep learning approach compared with human observers.

Approach: A total of 99 radiographs (blurry 57, nonblurry 42) were independently observed and rated by six observers using preview and diagnostic liquid crystal displays (LCDs). The deep convolution neural network (DCNN) was trained and tested using ninefold cross-validation. The average areas under the ROC curves (AUCs) were calculated for each observer with LCDs and by stand-alone DCNN for each test session and then statistically tested using a 95% confidence interval.

Results: The average AUCs were 0.955 for stand-alone DCNN and 0.827 and 0.947 for human observers using preview and diagnostic LCDs, respectively. The DCNN revealed a high performance for image motion blur on digital radiographs (sensitivity 94.8%, specificity 96.8%, and accuracy 95.6%), along with the capability to detect a slight motion blur that was overlooked by human observers with a preview LCD. There were no cases of motion blur overlooked by the stand-alone DCNN, of which some were incorrectly recognized as nonblurry by human observers.

Conclusions: The deep learning-based approach was capable of distinguishing slight motion blur that was unnoticeable on a preview LCD, and thus, is expected to aid the human visual system for detecting blurred images in the initial review of digital radiographs.

 [DOI: 10.1117/1.JMI.9.1.015501]

Keywords: motion blur; radiography; deep learning; ROC study; LCD monitor.

Paper 21264R received Oct. 2, 2021; accepted for publication Jan. 3, 2022; published online Jan. 18, 2022.

1 Introduction

In digital radiography (DR), body movements are one of the major causes in image retakes (11.99%), following positioning error (56.05%), and image artifacts (20.57%).[1] The necessity for image retakes is initially determined on a general-purpose liquid crystal display (LCD) equipped with an operating system and the image quality is checked on a diagnostic LCD, before storing it in the picture archiving and communication system. When lower-resolution monitors are used for the initial review, the image retake rate is reportedly approximately twice that for high-resolution monitors because image blurring is not observed on lower resolution monitors.[2] To avoid these issues, some DR systems are equipped with image analysis-based detection techniques for motion blur.[3–6]

*Address all correspondence to Rie Tanaka, rie44@mhs.mp.kanazawa-u.ac.jp

2329-4302/2022/$28.00 © 2022 SPIE

Blur detection methods can be divided into two categories: those based on traditional hand-crafted features and those based on deep learning neural networks (DCNNs). In the field of general radiology, there have been many attempts to detect image motion blur using methods based on traditional handcrafted features, such as edge sharpness and spatial frequency patterns,[7–11] along with a deblurring algorithm for burred images.[12,13] Due to their outstanding performance in high-level feature extraction and parameters learning, DCNNs have attained new state-of-the-art blur detection[14] and are expected to be an alternative to the human visual system for detecting motion blur in medical images.

Previous studies proposed a patch-level CNN and DCNN,[15,16] a multistream bottom-top-bottom fully convolutional network,[17] and a U-net-based CNN to learn blur features.[18,19] Although a deep learning-based approach is promising for detecting motion blur, its performance compared with visual assessment in DR remains to be determined. If such information is available, it could facilitate the implementation of deep learning-based approaches in clinical settings, as well as cooperation with humans in the radiology department.

The purpose of this study is to investigate the performance of image motion blur detection via a deep learning approach compared with that of human observers using two different LCDs. The study was designed to be based on receiver operating characteristic (ROC) analysis using motion phantom images with a known ground truth to ensure reliable quantitation.

2 Methods

2.1 *Dataset*

Body movements were simulated using a moving metronome (Model 221 NIKKO SEIKO). In this study, the tempo of the metronome was set to 40 beats per minute (bpm), simulating a patient's movement in the range of 0 to 20 cm/s, which covers the heart wall motion in 60 bpm (2 cm/s) and unexpected body motion (20 cm/s). Imaging was performed using a computed radiography (CR) system (FCR Velocity T, Fujifilm Corp., Tokyo, Japan), under imaging conditions for routine chest radiography (120 kV, 400 mA, source-image distance: 2.0 m) with auto exposure control (AEC). To adjust the exposure time under AEC, an acrylic board was placed in front of a moving metronome; the thicker acrylic board extended the exposure time, increasing the image noise and motion blur. The acrylic board thickness was set to 5.0, 7.5, 10, and 12.5 cm, resulting in exposure times of 5.0, 12.25, 23.0, and 42.5 ms, respectively, covering various exposure times for the average adult man in digital chest radiography. A total of 104 images—comprising 60 blurred and 44 nonblurred images—were obtained for this study. For each acrylic board thickness, 15 images of a moving metronome and 11 images of a metronome with a fixed pendulum (pendulum angle θ; $-50 \leqq \theta \leqq 50$ deg, $++10$) were obtained. The matrix size was 1760×1760 pixels, the pixel size was 100×100 μm^2, and the gray-scale image range was 10 bits. The amount of image motion blur was calculated by multiplying the motion speed of the tip of the pendulum by exposure time.

From the obtained images, a total of 99 images were used, for a test session in our observer study and training and testing the DCNN to detect motion blur. The remaining five images were only used for a pretraining session in the observer study. The images were classified into five groups, based on difficulty level, depending on the amount of image unsharpness due to motion blur (Table 1). Level 1 is less than the human visual discrimination ability. Level 2 is less than the LCD pixel pitch. Levels 3 and 4 are less than two and three times larger than the LCD pixel pitch, respectively; i.e., higher levels indicate facile image motion blur detection. Figure 1 shows the representative images for each difficulty level.

2.2 *Observer Study*

Images were observed on two LCD monitors with different screen resolutions; one is a diagnostic LCD (a 2M-monochrome monitor, native resolution: 1200×1600, viewable image size: 324.0 mm $\times$ 432.0 mm, pixel pitch: 0.270×0.270, brightness: 1000 cd/m^2) (EIZO RadiForce GS220, EIZO Corp., Japan) and the other is a preview LCD (a 1.3M-color all-purpose monitor,

Table 1 Criteria for the classification of degree of difficulty and the number of images in each level.

Degree of difficulty	Unsharpness U (mm)	Number of cases	Frequency (%)	
0	0	42	—	100
1	$0 < U \leqq 0.2$	21	36.8	
2	$0.2 < U \leqq 0.27$	8	14.0	
3	$0.27 < U \leqq 0.54$	15	26.3	100
4	$0.54 < U \leqq 0.81$	6	10.5	
5	$0.81 < U$	7	12.3	

Note: U, the amount of image unsharpness.

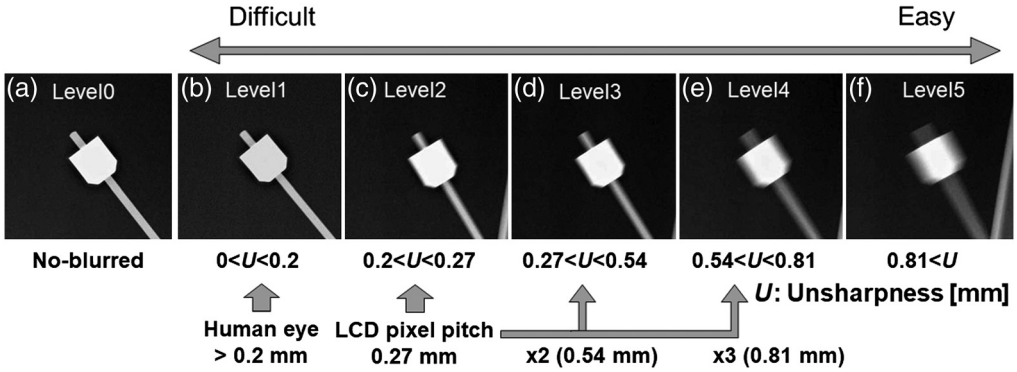

Fig. 1 Representative image at each difficulty level for detecting image motion blur. (a) level 0, static; (b) level 1, extremely difficult; (c) level 2, very difficult; (d) level 3, difficult; (e) level 4, relatively-easy; and (f) level 5, easy. U, the amount of image unsharpness; LCD, liquid crystal display.

native resolution: 1280×1024, viewable image size: 338.0 mm $\times$ 270.0 mm, pixel pitch: 0.264×0.264, brightness: 230cd/m^2) (EIZO FlexScan L565, EIZO Corp., Japan) attached to the CR system. The displayed sample image size on the diagnostic and preview LCDs were 298.9 mm $\times$ 298.9 mm (image resolution: 1200×1200) and 185.0 mm $\times$ 185.0 mm (image resolution: 700×700), respectively, which were determined via dedicated software for image viewing, respectively. Six radiographers with experience ranging from 1 to 10 years (mean, 2 years) participated in the ROC observer study.

The ROC observer study was conducted using a free ROC software (ROCViewerForMethod1Ver1.0.1) developed by the Japanese Society of Radiological Technology (JSRT) task group,[20] which follows the ROC curve-fitting software package developed by Metz et al.[21] The software provided the rating bar for determining a confidence of image blurring by clicking mouse on the bar, where the left and right ends corresponded to definitely nonblurry and definitely blurry, respectively. Rating scales were then converted with continuous values from 0.0 to 1.0 using a distance from the left end of the rating bar to the clicking point. We provided a pretraining session with five images that were not used in the main study and instructed observers how to use the rating bar of the software. Subsequently, followed by a pretraining session, randomized 99 images were independently observed and rated by the observers regarding the presence of image motion blur.

2.3 *Detection of Motion Blur with DCNN*

Table 2 presents the architecture of the DCNN used in this study. The DCNN was composed of four convolution layers, four pooling layers, and fully connected layers. The convolution layers

Table 2 Architecture of deep convolution neural network used to detect image motion blur.

Layer (type)	Output shape	Param #
input_1 (InputLayer)	(None, 256, 256, 1)	0
conv2d_1 (conv2D)	(None, 255, 255, 16)	272
max_pooking2d_1 (MaxPooling2D)	(None, 127, 127, 16)	0
activation_1 (activation)	(None, 127, 127, 16)	0
conv2d_2 (conv2D)	(None, 126, 126, 16)	4112
max_pooking2d_2 (MaxPooling2D)	(None, 63, 63, 16)	0
activation_2 (activation)	(None, 63, 63, 16)	0
conv2d_3 (conv2D)	(None, 62, 62, 16)	4112
max_pooking2d_3 (MaxPooling2D)	(None, 31, 31, 16)	0
activation_3 (activation)	(None, 31, 31, 16)	0
conv2d_4 (conv2D)	(None, 31, 31, 16)	2320
max_pooking2d_4 (MaxPooling2D)	(None, 15, 15, 16)	0
activation_4 (activation)	(None, 15, 15, 16)	0
flatten_1 (flatten)	(None, 3600)	0
dense_1 (dense)	(None, 1)	3601

used 16 filters with a 4×4 or 3×3 kernel while the pooling layers conducted subsampling that outputs the maximum value in a 2×2 kernel for every 2 pixels, reducing the matrix size of the feature map to half the size. Thus, after applying four convolution layers and four pooling layers, 16 of the 15×15 pixels two-dimensional feature map are input to the fully connected layer in a one-dimensional form. Sigmoid converted a value generated by the upstream processes to provide a sigmoid-converted value between 0.0 and 1.0, which was used as a rating score for motion blur. The last process of this architecture was BinaryCrossEntropy for binarization of the input data. The number of iterations, epochs, and batch size were set to 50, 100, and 32, respectively. Adams (learning rate = 0.001, beta1 = 0.9, beta2 = 0.999) was used as the optimization algorithm.[22] In this study, the DCNN was trained using the Sony Neural Network Console version 2.0 (Sony Network Communication Inc., Tokyo, Japan),[23] on Windows 10 and accelerated by a graphics processing unit (NVIDIA GeForce RTX 2080 Super with 8 GB of memory).

DCNN training and testing were performed using ninefold cross-validation to detect image motion blur. To prepare input data for the DCNN, a total of 99 square regions of interest (ROIs), each with 256 pixels, were cropped from the 99-image dataset (such that the pendulum was center-image) and then randomly divided into nine subsets to ensure similar image composition ratios at each difficulty level in each subset with those of the original ROIs. Here, a subset consisting of 11 images was used as the test data and the remaining eight subsets consisting of 88 images were used as training data (training:validation = 3:1). This subdivision process was conducted before data augmentation to ensure that the same original ROI images were not present in either the training or test data. The original ROIs in each subset were augmented by vertical and horizontal flipping, as well as by rotating the image angles from 0 deg to 30 deg, in 6-deg increments. This increased the amount of data by a factor of 24, resulting in 2112 images as training data (training : validation = 1584:528). The cross-validation process was repeated so each subset was used once as the test data and each test session was conducted using the original 11 images without data augmentation. The model accuracy was obtained by summarizing the test results. In this study, ninefold cross-validation was conducted six times, i.e., the same number as observers

who participated in the ROC observer study. The computation time on average for training and testing were 105.1 and 3.51 s, respectively. Before the experiments, we ensured that the training process effectively worked for learning the DCNN, using the learning curve (the loss value) and using t-distribution stochastic neighbor embedding plot of the feature space before and after training.[24] In addition, we conducted the classification using the k-means clustering method with $k = 2$ for the features obtained from the final layer of the DCNN with initialized weight values, to ensure no structure effect of the DCNN that often captures rich semantic features without any training.[25] We also performed the two-class classification (i.e., blurred and no-blurred images) using a support vector machine (SVM) algorithm,[26] to compare the classification accuracy based on the DCNN.

2.4 *Data Analysis*

The average areas under the ROC curves (AUCs) were calculated for each observer in each monitor, as well as for each test session by stand-alone DCNN using a free software developed by the JSRT task group (ROC Analyzer), where the binormal ROC model (JLABROC) was used for ROC curve fitting.[27] Statistical differences between the average AUC values were tested using 95% confidence intervals. Sensitivity, specificity, and accuracy were calculated for each approach. In addition, to compare average rating scores obtained by human observers and stand-alone DCNN, we used a paired t-test for each difficulty level. The statistical significance was set at $P < 0.05$.

3 Results

Figure 2 shows the scatter plot of k-means clustering ($k = 2$) before and after training. The DCNN with initialized weight values did not separate blurred and no-blurred images. After the training (epoch 100), although still not completely, the DCNN separated the images into two clusters. Figure 3 shows the ROC curves for six observers using preview and diagnostic LCDs, and for the results of six training sessions and testing of stand-alone DCNN. Figure 4 shows the average ROC curves for each approach. The average AUCs were 0.955 (95% CI: 0.950 to 0.960) for the stand-alone DCNN and 0.827 (95% CI: 0.804 to 0.849) and 0.947 (95% CI: 0.926 to 0.969) for human observers using preview and diagnostic LCDs, respectively. Although there was no significant difference in average AUCs between human observers with a diagnostic LCD and stand-alone DCNN, both were significantly larger than those of human observers with a preview LCD. Figure 5 shows the average values and standard deviation (SD) for the rating score obtained in our observer study and for those from the stand-alone DCNN for each difficulty level of motion blur. For blurred images (levels 1 to 5), human observers using a diagnostic LCD and stand-alone DCNN showed higher average ratings compared with those of human observers using a preview LCD, especially at the most difficult level (level 1). In addition, the stand-alone DCNN indicated a smaller SD of rating score compared with those of human observers with

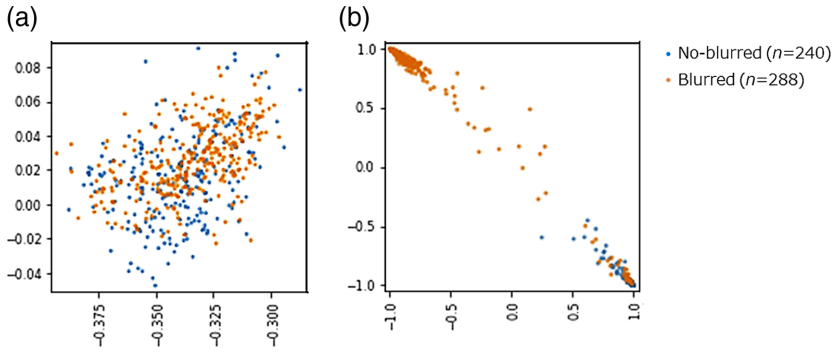

Fig. 2 The scatter plot of k-means clustering ($k = 2$) (a) before and (b) after training, showing the DCNN separates blurred and no-blurred images based on image features and not based on structure effect of the DCNN that often captures rich semantic features without any training.

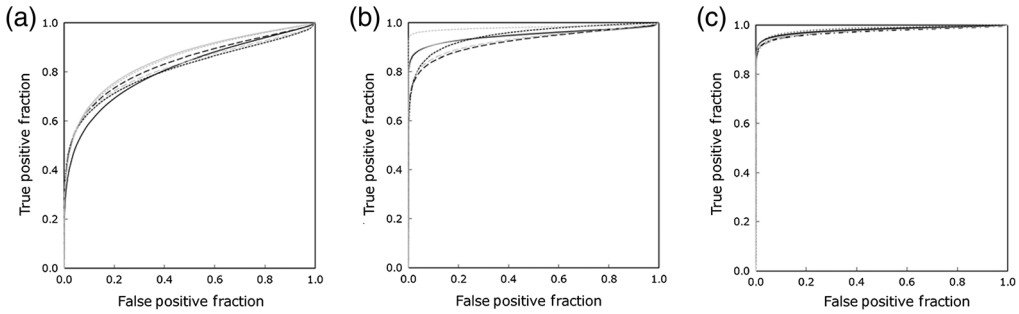

Fig. 3 ROC curves for six observers obtained using (a) preview LCD, (b) diagnostic preview LCD, and (c) six trainings and testing of stand-alone DCNN.

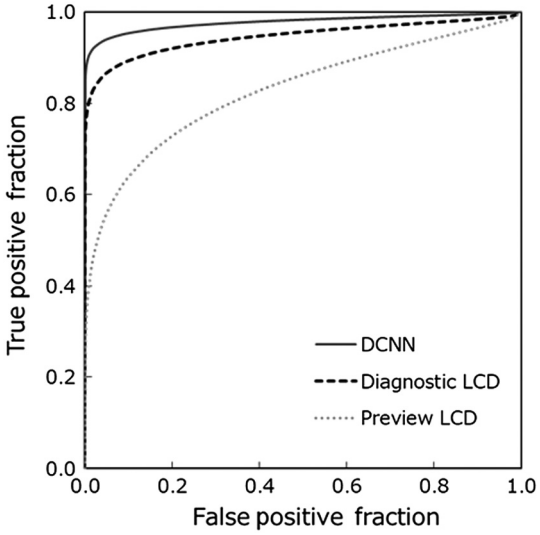

Fig. 4 Averaged ROC curves for six observers using preview and diagnostic LCDs and stand-alone DCNN.

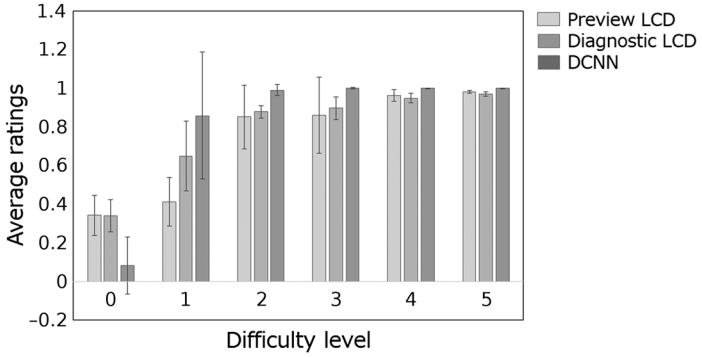

Fig. 5 Average ratings and SDs at each degree of difficulty. Error bars show ± SD. LCD, liquid crystal display; DCNN, deep convolutional neural network.

LCDs, except for slight image motion blur (level 1). Conversely, for no-blurred images (level 0), stand-alone DCNN indicated a significantly lower average rating score with a larger SD than human observers with LCDs ($P < 0.05$).

Table 3 presents the detection performance (sensitivity, specificity, and accuracy) for motion blur in each approach. The stand-alone DCNN revealed the best performance for detecting motion blur among the three approaches (sensitivity 94.8%, specificity 96.8%, and accuracy 95.6%). The classification accuracy of blurred and no-blurred images using the DCNN was

Table 3 Detection performance for motion blur in each approach.

	TP	TN	FP	FN	Sensitivity	Specificity	Accuracy
Preview LCD	44.2	26.3	15.7	12.8	77.5	62.7	71.2
Diagnostic LCD	53.7	28.7	13.3	3.3	94.2	68.3	83.2
Stand-alone DCNN	54.5	40.7	1.3	3.0	94.8	96.8	95.6
SVM	50.0	20.0	22.0	7.0	87.7	47.6	70.7

Note: TP, true positive; TN, true negative; FP, false positive; FN, false negative; LCD, liquid crystal display; DCNN, deep convolutional neural network; SVM, support vector machine.

higher compared with using the SVM (95.6% versus 70.7%). There were, on average, 12.8, 3.3, 3.0, and 7.0 cases with false-negative (FN) responses by human observers with preview and diagnostic LCDs, by the stand-alone DCNN, and the SVM, respectively. In addition, among the FN cases provided by human observers with a preview LCD, an average of 10.5 cases were correctly detected by the stand-alone DCNN. For no-blurred images (level 0), there were an average of 15.7 and 13.3 cases with false positive (FP) responses provided by human observers with preview and diagnostic LCDs, respectively, while an average of 1.3 and 22.0 FP cases was provided by the stand-alone DCNN and the SVM.

4 Discussion

The detection performance of the stand-alone DCNN for image motion blur was assessed by ROC analysis and compared to that of human observers using preview and diagnostic LCDs. Regardless of the amount of motion blur, the stand-alone DCNN exhibited a better performance than human observers with LCDs and also correctly detected subtle motion blur that was overlooked by human observers with a preview LCD. In addition, the stand-alone DCNN was able to correctly distinguish nonblurred images. These results confirm the usefulness of the DCNN for detecting motion blur in the initial review of DR.

There was a significant difference in the average AUCs between human observers with preview and diagnostic LCDs. This is thought to be due to the limited display size of a preview LCD. In general, the display size is restricted by the layout of the image-preview software equipped with an operating system. In this preview LCD case, the display size was limited to 185.0 mm × 185.0 mm, resulting in an image resolution of 700 × 700 pixels, which is much smaller than that of 1200 × 1200 pixels on a diagnostic LCD. Therefore, if a preview LCD was replaced with a diagnostic LCD, the image resolution could only be slightly improved as long as the display size of the image preview software is limited. In such a clinical situation, DCNN can aid blur detection in the initial review of digital radiographs. In fact, the stand-alone DCNN revealed higher AUCs than human observers using a preview LCD for the detection of motion blur. In addition, for motion blur that exceeded twice the LCD pixel pitch (levels 2 to 5 in this study), the DCNN provided higher ratings and a smaller SD than human observers with LCDs, suggesting that the DCNN could perform stably and effectively for this amount of motion blur. Furthermore, the DCNN revealed not only high sensitivity and specificity for image motion blur on digital radiographs but was also capable of detecting slight motion blur that was overlooked by human observers with a preview LCD. Moreover, there were no cases of motion blur overlooked by the stand-alone DCNN, of which some were incorrectly recognized as nonblurry by human observers. These results suggest that stand-alone DCNN could be an alternative to the human visual system for detecting motion blur in general radiography. High specificity of the DCNN for detecting motion blur might is also expected to improve throughput in the initial review using a preview monitor.

This study has some limitations. First, the present study assessed the motion blur of a moving pendulum image with sharp counter and high image contrast; this is easily detectable compared with human anatomy, with the various complex motion blurs observed in clinical images.

In addition, the ROI was manually set around the pendulum. Further studies are required to investigate deep learning-based blur detection in clinical images to reach a definitive conclusion. Second, the DCNN architecture used in this study is relatively simple. Furthermore, the number of image datasets used for training the DCNN was limited. In this study, we confirmed that the DCNN distinguished image blurring based on image features and not based on its structure effect using the *k*-means clustering method. Therefore, the detection performance for motion blur can be further improved by modifying the DCNN architecture and increasing the number of training datasets. Third, in this study, a 2M-monochrome monitor was utilized as a diagnostic LCD. An ROC observer study with a higher resolution monitor, such as a 5M-monochrome monitor, might provide more information for considering how to utilize deep learning in clinical practice.

Although the feasibility of a deep learning-based approach for blur detection in general radiology was ascertained, further studies are required to confirm the performance of the DCNN in clinical images of varying body movements, body parts, and sizes, under different imaging conditions. Such studies will pave the way for clinically implementing deep learning for detecting blurred images in the initial review of digital radiographs.

5 Conclusion

The deep learning-based approach was capable of distinguishing slight motion blur that was not observed on a preview LCD. Stand-alone DCNN revealed high sensitivity and specificity and worked stably for blur detection on digital radiographs. Further improvement could be achieved by improving the DCNN architecture and increasing the amount of training data. Deep learning is expected to aid the human visual system for detecting blurred images in the initial review in general radiography.

Disclosures

No conflicts of interest.

Acknowledgments

The authors thank Mrs. Miho Takamori from Ishikawa Prefectural Central Hospital, who assisted in data acquisition. They also thank Noriyuki Hashimoto from EIZO Corporation, who provided an LCD monitor.

References

1. C. S. Lin et al., "Guidelines for reducing image retakes of general digital radiography," *Adv. Mech. Eng.* **8**(4), 1–6 (2016).
2. W. K. Ma et al., "Blurred digital mammography images: an analysis of technical recall and observer detection performance," *Br. J. Radiol.* **90**(1071), 20160271 (2017).
3. T. Kawamura, "Body motion detection device and method," US patent US14/666,468.
4. J. Yamamoto et al., "Radiograph Processing device for medical use, and radiography device," WO/2019/064351, PCT/JP2017/034797.
5. Y. Matsumoto, "Medical image photographing system, medical image processing apparatus, and program," JP2011247358A.
6. V. A. Venkatesan et al., "Method and system for reducing motion blurring in digital radiography," US patent US9418405B2.
7. M. L. Hill et al., "Development of an automated detection algorithm for patient motion blur in digital mammograms," *Proc. SPIE* **10718**, 107180K (2018).
8. Y. Tanabe et al., "Automated detection of respiratory movements for image quality assurance," *J. Med. Imaging Health* **10**(7), 1473–1478 (2020).
9. N. Komona et al., "Automatic detection of simulated motion blur in mammograms," *Med. Phys.* **47**(4), 1786–1795 (2020).

10. K. A. Mohan et al., "SABER: a systems approach to blur estimation and reduction in x-ray imaging," *IEEE Trans. Image Process.* **29**, 7751–7764 (2020).
11. H. Luo et al., "Motion blur detection in radiographs," *Proc. SPIE* **6914**, 69140U (2008).
12. A. A. Abdulmunem et al., "A deep learning-based scatter correction of simulated x-ray images," *Electronics* **8**(9), 944 (2019).
13. J. Hori et al., "Band-suppressed restoration of x-ray images blurred by body movement," *Methods Inf. Med.* **39**(2), 130–133 (2000).
14. H. Fujita, "AI-based computer-aided diagnosis (AI-CAD): the latest review to read first," *Radiol. Phys. Technol.* **13**, 6–19 (2020).
15. J. Park et al., "A unified approach of multi-scale deep and hand-crafted features for defocus estimation," in *Proc. IEEE Conf. Comput. Vision and Pattern Recognit.*, pp. 1736–1745 (2017).
16. R. Huang et al., "Multiscale blur detection by learning discriminative deep features," *Neurocomputing* **285**, 154–166 (2018).
17. W. Zhao et al., "Defocus blur detection via multi-stream bottom-top-bottom fully convolutional network," in *IEEE/CVF Conf. Comput. Vision and Pattern Recognit.*, pp. 3080–3088 (2018).
18. O. Ronneberger et al., "U-net: convolutional networks for biomedical image segmentation," *Lect. Notes Comput. Sci.* **9351**, 234–241 (2015).
19. X. Xiao et al., "MSDU-net: a multi-scale dilated U-net for blur detection," *Sensors* **21**, 1873 (2021).
20. J. Shiraishi et al., "Basic concepts and development of an all-purpose computer interface for ROC/FROC observer study," *Radiol. Phys. Technol.* **6**(1), 35–41 (2013).
21. C. E. Metz et al., "Maximum likelihood estimation of receiver operating characteristic (ROC) curves from continuously-distributed data," *Stat. Med.* **17**, 1033–1053 (1998).
22. D. P. Kingma et al., "Adam: a method for stochastic optimization," arxiv.org/abs/1412.6980 (2017).
23. "Neural network console," https://dl.sony.com// (accessed 16 June 2021).
24. L. van der Maaten and G. Hinton, "Visualizing data using t-SNE," *J. Mach. Learn. Res.* **9**, 2579–2605 (2008).
25. S. Saha et al., "Deep no learning approach for unsupervised change detection in hyperspectral images," *ISPRS Ann. Photogramm. Remote Sens. Spatial Inf. Sci*. **V-3-2021**, 311–316 (2021).
26. W. Noble, "What is a support vector machine?" *Nat. Biotechnol.* **24**, 1565–1567 (2006).
27. J. Shiraishi et al., "Verification of modified receiver-operating characteristic software using simulated rating data," *Radiol. Phys. Technol.* **11**(4), 406–414 (2018).

Rie Tanaka is an associate professor of radiological technology at Kanazawa University in Japan. She received her PhD in health sciences from Kanazawa University. She has been working on research and development of dynamic chest radiography, that is, flat-panel detector-based functional lung imaging, along with its clinical evaluation. Her research interests also include virtual imaging trials using XCAT phantom and observer study.

Juni Shiraishi is a professor of faculty of life sciences at Kumamoto University in Japan. He received his PhD in engineering from Osaka City University. He had been belonging to the Kurt Rossmann Laboratories in the University of Chicago from 2001 to 2009. He has been working on research and development of computer-aided diagnosis systems for radiologic images as well as a practical evaluation of their clinical utility using observer studies such as ROC and FROC.

Biographies of the other authors are not available.